RESEARCH

Rate-dependent constitutive modelling blasting crack initiation and propagation in rock masses

Yongjun Zhang[1] · Meng Xu[1,2] · Sijia Liu[1] · Fei Liu[1] · Qingsong Wang[3]

Abstract

This study examines the fracture mechanism of cracks and the final blasting effects on defective rock masses under blasting loads. The failure processes of jointed rock with two prefabricated joints are investigated through numerical simulations using a two-dimensional finite element method. Subsequently, simulations are performed to analyze the blasting of granite specimens with various joint arrangements, focusing on the influence of front joint length, inclination angle, and blast hole distance on failure patterns, displacement, velocity, and stress at the joint ends. The numerical results provide a comprehensive summary of various typical failure modes near blast holes and joints for the first time. Specifically, the simulation successfully captures the characteristics of the ring crack zone, wing cracks, and main crack deflection affected by the front joint. Moreover, the results highlight the shielding effect of the front joint, which enhances damage in the medium between the borehole and the joint while exhibiting the opposite effect behind the joint in terms of stress wave propagation. Overall, this study offers objective insights into the mechanics and failure characteristics of jointed rock masses under blasting loads and serves as a valuable reference for the design and optimization of blasting operations.

Keywords Blasting failure · RHT model · Double-jointed granite specimen · Dynamic crack propagation · Stress wave spreading

Yongjun Zhang and Meng Xu contributed equally to this work.

✉ Sijia Liu
   liusijialyg@126.com

   Yongjun Zhang
   zyjun@qut.edu.cn

   Meng Xu
   xumengliqut@126.com

   Fei Liu
   liufei@qut.edu.cn

   Qingsong Wang
   10972076@qq.com

1   School of Civil Engineering, Qingdao University
    of Technology, Qingdao 266033, China

2   China State Construction Engineering Corporation
    International Construction CO., LTD., Suzhou 215011,
    China

3   CRCC Plateau Tunnel Construction Technology
    and Equipment R&D Center, China Railway 20th Bureau
    Group Corporation, Xi'an 710016, China

1 Introduction

Blasting serves as a widely employed technique for rock fragmentation in coal mining operations. However, natural rock formations, including coal deposits, often exhibit various discontinuities such as voids, joints, and faults, which have a substantial influence on the propagation and attenuation of stress waves (Huang et al. 2015; Wang et al. 2022; Raina 2019). Consequently, these discontinuities can significantly alter both the mode of crack propagation and the ultimate blasting effect (He et al. 2021). The comprehension of stress distribution and crack propagation within jointed rock masses becomes imperative when investigating dynamic fracture mechanisms under blasting loads in the realm of coal science.

In recent years, various theoretical studies have been conducted on the propagation of explosion-induced cracks in rock masses. From the perspective of the rock medium's response, the dominant factor leading to blasting failure is often attributed to the tensile effect resulting from the reflection of blast stress waves (Xie et al. 2017; Yang et al. 2017). Due to the lower tensile strength of rock-like

materials compared to compression, circumferential cracks are frequently initiated under tensile stress, particularly in the vicinity of free surface areas (Banadaki and Mohanty 2012; Xu et al. 2021). To examine the mechanism of blasting-induced cracks under the influence of blasting stress waves, various failure criteria have been employed, such as the Mohr-Coulomb criterion and the maximum tensile stress criterion. Ming et al. (2009) and Li and Ma (2010) established the wave propagation equation to study the interaction between shock waves and rock joints, taking into account the influence of confining pressure in deep rock masses. In addition to the aforementioned reflected tension waves, explosive gases have been recognized as playing a significant role in rock blasting (Yang et al. 2016; Yi et al. 2016; Yuan et al. 2019). These gases penetrate into cracks formed by shock waves, expand in the confined spaces, and generate pressure loading, thereby promoting and accelerating crack propagation. Previous studies (McHugh 1983; Daehnke et al. 1997) have indicated that the effect of gas pressure may even be more pronounced than that of stress waves in containment conditions. Furthermore, several dynamic fragmentation models based on fracture mechanics have been proposed to describe the morphology of rock cracks and evaluate the impact of blasting. Torbica and Lapcevic (2014) improved a fragmentation model for rock fractures, enabling the estimation of the density of tensile cracks and the radius of the fracture zone. Dai et al. (2010) and Zhang and Zhao (2013) applied quasi-static fracture mechanics theory to rock testing, providing a means to determine dynamic stress intensity factors. The accumulated knowledge from these studies contributes to a comprehensive understanding of rock blasting and paves the way for improved techniques and safety measures in the field.

However, the prediction and analysis of cracks become more complex when considering the heterogeneity of the rock mass, especially with the inclusion of joints. In response to this challenge, numerous researchers have conducted laboratory experiments on rocks (Zhang et al. 2021; Chi et al. 2019; Wang et al. 2020) or rock-like materials (Yang et al. 2008; Wang et al. 2016) to investigate the process of fragment bursting under various complex conditions. Theoretical studies of rock blasting are generally consistent with the observed crack propagation phenomenon in tests. However, the prediction and analysis of cracks become more complex when considering the heterogeneity of the rock mass, especially with the inclusion of joints. In response to this challenge, numerous researchers have conducted laboratory experiments on rocks (Zhang et al. 2021; Chi et al. 2019; Wang et al. 2020) or rock-like materials (Yang et al. 2008; Wang et al. 2016) to investigate the process of fragment bursting under various complex conditions. Zhang et al. (2021, 2020b) studied the effect of cylindrical granite samples on rock fracture under different stemming conditions.

Chi et al. (2019) reported a series of cylinder tests on granite cylinders with a central charge in a closed explosion room to study the pressure and attenuation of shock waves in granite. In Wang's research (Wang et al. 2020), the damage and degree of damage of small-sized specimens after blasting with an uncoupled charge in the chamber were qualitatively assessed, and the relationship between the uncoupled coefficient and the blasting effect was examined. Furthermore, some experiments (Liu and Qu 2014; Li et al. 2018, 2021; Miranda et al. 2013; Chen et al. 2018) were conducted on jointed rock samples to study the effects of discontinuous structures on blasting failure and the propagation laws of stress waves. Using PAMM as the experimental material, Yang et al. (2008) and Wang et al. (2016) designed experiments on prefabricated jointed rock masses to study the crack propagation behavior at the joint tips and the distribution of the surrounding stress field at the end of defects through the dynamic caustics method. Yang (2008) proposed a field test procedure for jointed rock masses and concluded that joints significantly affect the characteristics of stress wave propagation, such as peak attenuation, frequency spectrum, and spatial variation. Renshu et al. (2016) and Hao et al. (20012001) studied the shielding effect of joints on crack propagation through laboratory experiments and obtained the dynamic stress intensity factor formed at the joints and the propagation trend of the crack propagation speed under the action of blasting stress.

In recent years, various numerical methods, including the Finite Element Method (FEM) (Liu et al. 2019; Chao et al. 2020), Finite Difference Method (FDM) (Zhu et al. 2007, 2008; Wang et al. 2017), Discrete Element Method (DEM) (Hajibagherpour et al. 2020), Smoothed Particle Dynamics (SPH) (Gharehdash et al. 2020), hybrid methods (Yuan et al. 2018; Wang et al. 2021), and non-local damage models (Liu et al. 2022; Wang et al. 2023), have been widely employed to study the dynamic failure response of rock masses. Researchers such as Zhang et al. (2020a) and Siamaki et al. (2018) have utilized the particle-based DEM (PFC) methodology to simulate rock blasting and analyze the effect of blasting vibration on the degradation of joint shear strength. While discrete methods are suitable for modeling cracks, they require additional parameter calibration and are challenging to extend to elastoplastic behaviors. Continuous methods such as FEM and FDM make up for the deficiencies of discrete element methods in the complex constitutive model, allowing them to reproduce the blast processing of complex structures and the nonlinear characteristics of materials (Dai et al. 2022). Furthermore, hybrid methods combine the advantages of both continuous and discrete methods, making them a valuable tool for studying rock blasts (Wang and Konietzky 2009). In this work, we focus on the FEM approach implemented in the commercial software LS-DYNA, which has become one of the promising

numerical tools for studying rock blast damage (Hongtao et al. 2015; Ainalis et al. 2017; Zhang et al. 2016; Yi et al. 2021). For this numerical method, a reasonable damage evolution law and constitutive model are crucial in dealing with discontinuous structures such as nucleation, propagation, coalescence, and fragmentation. At present, a series of constitutive models (e.g., RHT, HJC) have been implemented in the finite element framework to conduct numerical studies on various explosion-induced failures, such as the blasting problem under in-situ stress (Jayasinghe et al. 2019), porous blasting processes (Xie et al. 2017), explosion-induced crack propagation (Yi et al. 2018), and damage evolution and spatial distribution (Wang et al. 2019).

Despite the noteworthy contributions in the field, studying the blasting response of jointed rock mass is still a challenging subject, especially when it comes to the influence of joints on stress wave propagation and the propagation of rock crack damage, which is rarely considered. Hence, this study aimed to address this knowledge gap by conducting a series of numerical experiments on crack propagation in rock masses with varying combinations of double joints. The objective was to investigate the mechanical behavior of crack propagation and the distribution of stress waves in jointed rock masses under blasting loads. By analyzing changes in the stress field and failure patterns caused by different joint arrangements, we reveal the general law of explosive crack propagation and failure models. The results of this study provide a reference for understanding the mechanical and failure characteristics of fissured rock mass defects under blasting loads.

This paper is organized as follows: In Sect. 2, we briefly state the different constitutive equations of the numerical methodology and algorithm of fluid-solid coupling. In Sect. 3, we establish three series of RHT granite models and simulate the failure processes of jointed rocks with different joint arrangements under blasting. Furthermore, we quantitatively explore the effects of joint length, inclination, and distance from the blasting hole on the mechanical and failure characteristics of jointed granite specimens in Sect. 4. Finally, we draw conclusions and summarize our findings in Sect. 5.

2 Numerical modeling of rock blasting

2.1 Constitutive models for blasting simulation

For numerical studies of blasting problems involving nonlinearities and large deformations, choosing a reasonable material model is crucial to the numerical results. LS-DYNA software provides many constitutive models for simulating rocks or rock-like materials. In this numerical study, the RHT model and the JWL equation of state will be employed to model the mechanical response of rock under blast loading. These models will be discussed below.

2.1.1 RHT constitutive model for rock material

The RHT constitutive model was proposed by Riedel, Hiermaier, and Thomas in 1998, based on previous research on the mechanical properties of concrete (Sparks and Menzies 1973; Rostasy et al. 1984; John et al. 1992), which embeds pressure-related elastic limit surface equations, failure surface equations, and residual strength surface equations (Shu et al. 2022).The model incorporates various parameters and equations to describe the fracture process, taking into account factors such as stress state, strain rate, and material properties. As illustrated in Fig. 1, the material is assumed to be elastic when the pressure P is lower than the pressure at which the material pores begin to crush P_{crush}. Once P exceeds P_{crush}, the pore
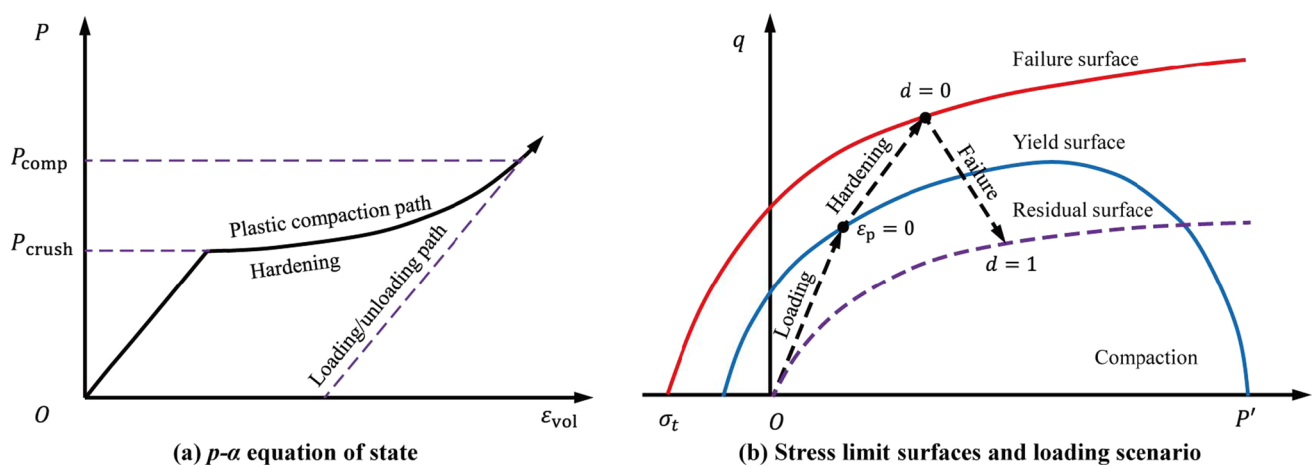

Fig. 1 RHT model (Borrvall and Riedel 2011): **a** Schematic description of the $p - \alpha$ EOS; **b** Stress limit surfaces and loading scenario

collapses, resulting in a decrease in the effective volume modulus of the material. If the pressure P_{crush} is between P and the pressure at which the material's pores are compacted P_{comp}, the material is assumed to be plastic. Moreover, the material will only yield if the load exceeds its yield limit, given a specific stress state and loading rate. It has been widely applied in studies related to impact and explosion dynamics, allowing researchers to better understand and predict the fracture behavior of brittle materials under dynamic loading conditions.

In the RHT model, the equations of state for $p - \alpha$ compaction of rock masses are:

$$P_R = \left[(B_0 + B_1\mu)\alpha_0\rho_0 e + A_1\mu + A_2\mu^2 + A_3\mu^3 \right]/a_0 \qquad (1)$$

where P_R represents the pressure of the equation of state (EOS) used in the RHT model, with material constants B_0 and B_1, initial porosity of the rock α_0, initial density of rock ρ_0, internal energy per unit mass e, and volumetric strain μ. To determine the polynomial coefficients, the following expressions can be used: A_1, A_2, and A_3:

$$A_1 = \alpha_0\rho_0 c_0^2 = T_1 \qquad (2a)$$

$$A_2 = \alpha_0\rho_0 c_0^2(2k - 1) \qquad (2b)$$

$$A_3 = \alpha_0\rho_0 c_0^2(3k^2 - 4k + 1) \qquad (2c)$$

where, c_0 is the sound speed at ambient pressure and temperature; T_1 is the material constant, and k is the empirical constant of the material.

The RHT model also includes a description of the hydrostatic pressure using the polynomial Hugoniot curve and the $p - \alpha$ compaction relationship, as shown in Fig. 1b. To describe the model's yield surfaces, compressive strength, regularized yield functions, and William-Warnke functions are utilized (Riedel et al. 1999):

$$\sigma_y\left(P_0^*, \dot{\varepsilon}_p, \varepsilon_p^*\right) = f_c\sigma_y^*\left(P_0^*, F_r(\dot{\varepsilon}_p), \varepsilon_p^*\right)R_3\left(\theta_l, P_0^*\right) \qquad (3)$$

where, σ_y^* denotes the standard yield function; f_c stands for the uniaxial compressive strength; R_3 represents the William-Warnke function, and θ_l denotes the pulse angle. Furthermore, the equation includes the dynamic strain rate increase factor, F_r, the normalization pressure, P_0^*, defined as $P_0^* = P_0/f_c$, hydrostatic pressure, P_0, strain rate ε_p, and the effective plastic strain rate $\dot{\varepsilon}_p$.

Thus, Failure surfaces indicate (Johnson and Holmquist 1994):

$$\sigma_f^*\left(P_0^*, F_r\right) = A_1\left[P_0^* - F_r/3 + \left(A_a/F_r\right)^{-1/N_1}\right]^{N_1} \qquad 3P_0^* \geq F_r \qquad (4)$$

where, $\sigma_f^* = \sigma_f/f_c$ is the normalized strength; A_1 and N_1 are the failure surface parameters.

The residual strength surface describes the strength of the broken concrete, which is related to the confining pressure state of the material. So, the residual strength surfaces can be described as follows:

$$\sigma_{res} = B * (P^*)^M \qquad (5)$$

where, B is the residual failure surface constant; M is the residual failure surface index, and P^* is the normalized hydrostatic pressure.

As the stress state of a material approaches its ultimate strength on the destruction surface, any further inelastic deformation or plastic strain results in a gradual accumulation of damage. In the event of destruction, the amount of plastic strain can be used to determine the extent of the damage. It should be noted that the plastic strain in case of failure is represented by:

$$\varepsilon_p^f = \begin{cases} D_1\left[P_0^* - (1 - D_r)P_t^*\right]^{D_2} & P_0^* \geq (1 - D_r)P_t^* + \left(\varepsilon_p^m/D_1\right)^{1/D_2} \\ \varepsilon_p^m & P_0^* < (1 - D_r)P_t^* + \left(\varepsilon_p^m/D_1\right)^{1/D_2} \end{cases} \qquad (6)$$

where ε_p^f represent the plastic strain at failure, ε_p^m is the minimum damage residual strain, P_t^* is the failure end pressure, D_r is a damage variable for the RHT model, D_1 and D_2 injury constants.

Finally, the damage variable D_r is defined as the accumulation of plastic strain as:

$$D_r = \sum \frac{d\varepsilon_p}{\varepsilon_p^f} \qquad (7)$$

2.1.2 Constitutive parameters of coupling material air

As a wildly used coupling material, the air model is described as a linear elastic model in this research. It uses the material with the keyword *MAT_NULL, the equation of state is represented by the keyword EOS_LINEAR_POLYNOMIAL (Hallquist et al. 2006), and the pressure is determined by the following form:

Table 1 Parameters of constitutive model for air

Density (g/cm^3)	C_0	C_1	C_2	C_3	C_4	C_5	C_6	Elastic modulus (MPa)
0.0012	0	0	0	0	0.4	0.4	0	0.0025

Table 2 Parameters for the explosive material

Density (g/cm^3)	A	B	R_1	R_2	ω	E (kJ/m^3)	V (m^3)
1.5	6.25	0.23	5.25	1.6	0.28	0.0864	1

$$P = C_0 + C_1\mu + C_2\mu^2 + C_3\mu^3 + \left(C_4 + C_5\mu + C_6\mu^2\right)E_0 \tag{8}$$

where $\mu = \rho/\rho_0 - 1$, ρ is the density, ρ_0 is the starting density, E_0 is the energy density of the beginning, $C_0, C_1, C_2, C_3, C_4, C_5$, and C_6 are parameters in the equation as listed in Table 1.

2.1.3 Dynamic loading produced by explosives

During blasting, explosives undergo rapid chemical reactions that can be described by various equations of state. One commonly used model is the Jones-Wilkins-Lee (JWL) EOS, which accurately predicts pressure changes resulting from blasting (Hallquist et al. 2006; Alia and Souli 2006). In this study, we employed the JWL_EOS to describe the blasting process, and the blast pressure was calculated using the following equation:

$$p = A\left(1 - \frac{\omega}{R_1 V}\right)e^{-R_1 V} + B\left(1 - \frac{\omega}{R_2 V}\right)e^{-R_2 V} + \frac{\omega E}{V} \tag{9}$$

where, V is the relative volume; E is the initial internal energy per unit volume of explosives, A, B, R_1, R_2, and ω are all parameters of the JWL equation of state as listed in Table 2.

2.1.4 Material parameters of joint

The keyword ∗MAT_PLASTIC_KINEMATIC describes isotropic hardening and follow-up hardening plastic models, commonly used as the constitutive structure of rock in rock mass blasting simulations (Hallquist et al. 2006), and the radius of the yield surface under this model is the initial yield strength plus hardening reads:

$$\sigma_y = \sigma_0 + \beta E_p \varepsilon_{eff}^p \tag{10}$$

Table 3 Parameters for the Joint material

Density (g/cm^3)	E (GPa)	c	σ_y (GPa)	E_t (GPa)	β
1.16	0.2	0.3	0.025	0.04	0.5

σ_y is yield strength, σ_0 is the initial yield strength, E_p is a plastic hardening modulus, ε_{eff}^p is an effective plastic strain.

The modulus of plastic hardening is given by the following equation

$$E_p = \frac{E_t E}{E - E_t} \tag{11}$$

E is the modulus of elasticity and the E_t is the tangent modulus.

According to the different β values, it can be used to describe various hardening models: when $\beta = 0$, it is follow-up hardening, the yield surface size is unchanged, and it moves in the direction of plastic strain; When $\beta = 1$, it is isotropic hardening, the position of the yield surface is unchanged, and the size changes with strain, at $0 \leq \beta \leq 1$, it is mixed hardening. Moreover, the Cowper–Symonds model is used in the ∗MAT_PLASTIC_KINEMATIC model to consider the effect of strain rate as follows:

$$\sigma_y = \left[1 + \left(\frac{\dot{\varepsilon}}{c}\right)^{1/p}\right]\sigma_0 \tag{12}$$

where, p and c are the parameters related to the strain rate, which is determined by the strain rate characteristics of the material; $\dot{\varepsilon}$ is the load strain rate.

Then the ∗MAT_PLASTIC_KINEMATIC model can be expressed as follows:

$$\sigma_y = \left[1 + \left(\frac{\dot{\varepsilon}}{c}\right)^{1/p}\right]\left(\sigma_0 + \beta E_p \varepsilon_{eff}^p\right) \tag{13}$$

The specific parameters for joint material are listed in Table 3.

2.2 Algorithm of fluid–solid coupling

The finite element method (FEM) is a powerful and robust numerical technique for simulating the progressive failure of rock materials and revealing the fracture and fracture mechanisms of rocks under dynamic loading (Zhang et al. 2019; Liu et al. 2021). In FEM, there are three basic algorithms for three-dimensional elements: Lagrangian, Eulerian, and Arbitrary Lagrange-Eulerian Algorithm (ALE), which are controlled by THE ELFORM keyword in *SECTION_SOLID. The Lagrange algorithm attaches elements to the material, enabling deformation to be generated with the flow of the material. However, numerical difficulties can arise when the structure undergoes large deformation, particularly due to high-stress gradients at the failure interface, which often causes the simulation to break down before analysis is complete because of convergence issues associated with topological changes. In contrast, the Euler algorithm is suitable for computational analysis of fluid mechanics and explosion of explosives in the rock mass, but it results in a longer and more complicated calculation process for the model. Therefore, to overcome the limitations of the Lagrangian and Eulerian formulations, the ALE algorithm, which couples both formulations, is used for fluid–structure interaction analysis in this research.

The basic principles of the ALE algorithm involve performing one or several Lagrange time-step calculations, during which the element mesh deforms with the flow of material, followed by an ALE time-step calculation consisting of (1) maintaining the boundary conditions after the object's deformation and remeshing the interior, and (2) transporting the element variables and node velocity vectors from the deformed mesh to the repartitioned mesh.

As shown in Fig. 2, the rock is solid, and explosives and air are fluids. Therefore, The explosive and air parts are controlled by ALE formulation based on the common nodes, while the rock belongs to the Lagrange algorithm. If only explosives and rocks are set up, the rocks will not be damaged, and the model is also a failure. The coupling between explosives, air, and rocks is the formation of a domain of air between rocks and explosives as a medium. The energy waves generated by the explosion of explosives are transmitted to the rock through the air medium, thus acting on the rock and causing destructive damage to rock. Currently, coupling algorithms have been widely used in finite element analysis, especially in the explosion of structures. The interaction effect between structural elements and fluids using the LAGRANGE algorithm is achieved by defining the keyword *CONSTRAINED_LAGRANGE_IN_SOLID, and the numerical model of the target structure and fluid and the element grid can overlap. The methods of coupling the target structure to the fluid are: acceleration, velocity, penalty function, and other constraints to accomplish the interaction between the fluid and the solid.

3 Numerical simulations

In this section, we explore the blasting response of a jointed rock mass using the constitutive model and parameters introduced in Sect. 2. First, we present a benchmark of granite specimens with a single borehole for numerical validation. Then, we conduct a series of numerical experiments with two joints to investigate the effect of joint arrangements. All numerical experiments are carried out under a two-dimensional plane strain assumption.

Fig. 2 Algorithm of the fluid-solid coupling with explicit time integration in ALE

Dynamite (ALE)

Rock (Lagrangian)

Air (ALE)
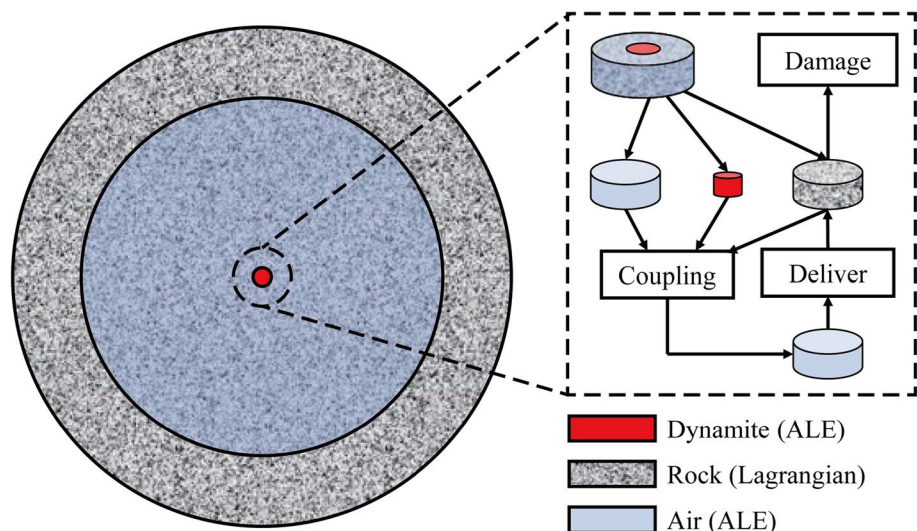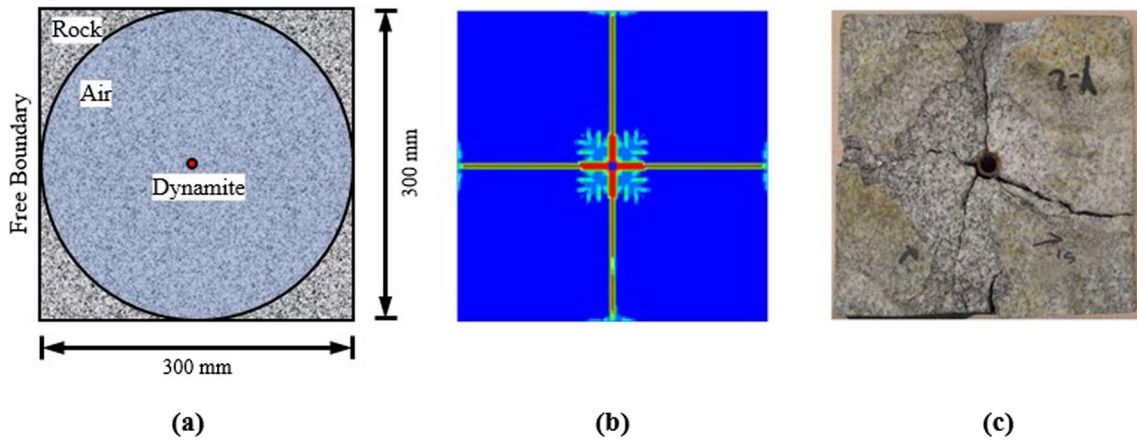
Fig. 3 Schematic diagram for borehole blasting experiment: **a** geometric and boundary conditions, **b** ultimate failure pattern predicted by numerical test, and **c** the failure pattern observed in experiment of the Barre granite (Banadaki and Mohanty 2012)

Table 4 Parameters of RHT model for granite

Parameter	Value	Parameter	Value	Parameter	Value
ρ_0(kg/m^3)	2700	F_t^*	0.05	β_t	0.036
G (GPa)	0.219	F_s^*	0.18	G_c^*	1
f_c (MPa)	1.67	A_1 (GPa)	0.257	G_t^*	0.7
N_1	0.76	A_2 (GPa)	0.3784	XI	0.5
β_c	0.032	A_3 (GPa)	0.2129	D_1	0.04
B_0	1.22	Q_0	0.567	D_2	1
B_1	1.22	B_q	0.05	P_{crush} (MPa)	1.25
α_0	1	A	2.44	A_f	0.25
T_1 (GPa)	0.257	N_p	0.76	N_f	0.6
T_2 (GPa)	0	P_{lock} (GPa)	0.06		

3.1 Calibration of the RHT model

For the first case, we conducted a numerical simulation of single-hole blasting on a standard square specimen made of granite. The specimen has a length of 300 mm and is discretized into 22,500 quadratic quadrilateral elements with uniform size ($h_e = 2$ mm). Additionally, we created a circular air domain consisting of approximately 17,663 elements and an explosion source consisting of 4 elements, as shown in Fig. 3. To prevent the propagation of reflected tensile cracks, we applied non-reflecting boundary conditions around the model.

The geometric setup for the borehole blasting experiment, including the rock, explosives, and air, is depicted in Fig. 3a. Microscopic parameters of the simulated granite's RHT model are determined in Table 4 based on previous laboratory experiments using the split Hopkinson pressure bar (SHPB) test of granite (Li 2016).

The predicted crack growth paths under explosive loading conditions are shown in Fig. 3b. As depicted in the figure, a crushed zone emerges around the borehole, and four radial cracks propagate towards the outer boundary of the rock specimen. Moreover, the ultimate failure patterns of the Barre granite in the blasting test obtained from the previous experimental observations (Banadaki and Mohanty 2012) are compared to the numerical results, as demonstrated in Fig. 3c. It can be seen that the presented numerical results are in good agreement with the previous experimental findings, which suggests that our numerical model and its parameters are capable of reproducing the mechanical and failure behaviors of granite.

3.2 Setup for the blasting experiment

In this numerical study, parallelepiped granite specimens with dimensions of 400 mm × 500 mm × 2 mm are used. The filling medium is also granite. Two prefabricated joints are created in the intact granite specimen by replacing the material model. The front joint (Joint A) is located at the center of the specimen and has a width of 4 mm. As shown in Fig. 4a, the length of Joint A is denoted by L, the distance from the center of Joint A is denoted by D, and α represents the joint inclination angle. Another horizontal joint (Joint B) is located 30 mm away from Joint A to study the dynamic propagation of rock defects under diffraction waves. Its length and width are fixed at 80 mm and 4 mm, respectively. An explosive (2.7 g/cm^3 and 4 mm in diameter) is placed on the left side of Joint A to simulate the formation of blast loads. To eliminate the stress wave reflection from the outer boundaries, a non-reflection boundary is adopted in the outer boundaries of the model.
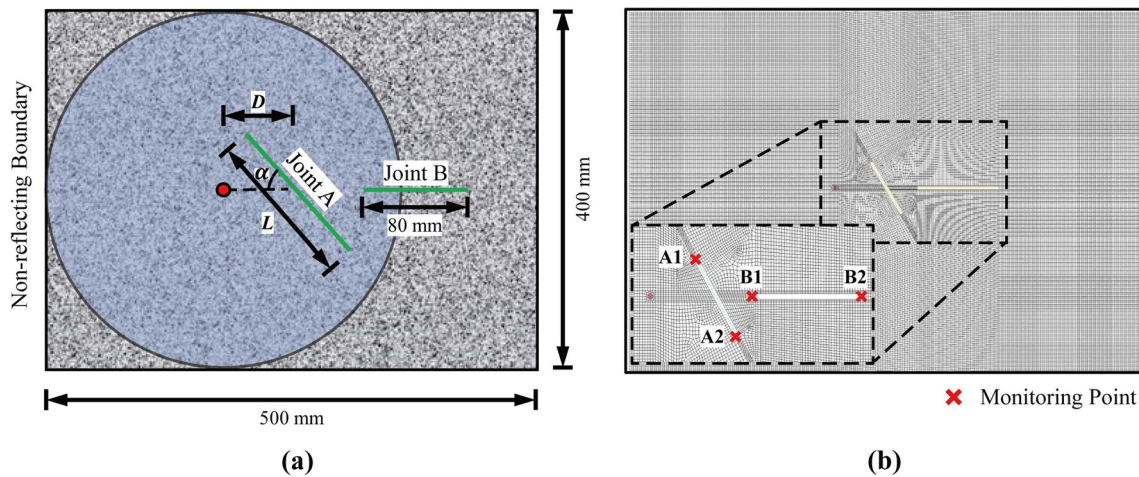
Fig. 4 Schematic diagram for borehole blasting experiment. **a** Geometric and boundary conditions and **b** the finite element discretization

Table 5 Geometric parameters of prefabricated joints in numerical granite specimens

Joint length (mm)	Joint angle (°)	Blast hole distance (mm)
0	0	25
20	30	50
40	45	70
60	60	90
80	90	100

In the numerical simulation, 50,000 8-node elements for a total of 400,000 nodes with uniform size ($h = 2$ mm) are used to discretize the computational domain, as shown in Fig. 4b. Four monitoring points (A1, A2, B1, B2) are set at the wing end element with two prefabricated joints.

In this numerical research, the stress wave propagation process is accomplished by setting a coupling of rock, air, explosives, and joints. Since the discontinuous structural planes in natural rock masses usually appear in the form of closed fractures, filler-based joints are used that are first dug out and then filled with medium.

In order to study the fracture characteristics of joint rock mass under blasting load, a total of 13 study cases were studied, and the following three groups of parameters were considered, as listed in Table 5.

(1) When the inclination angle α of Joint A is fixed at 90° and blast hole distance D is 50 mm, increase the length L of Joint A from 0 to 80 mm with an interval of 20;
(2) Joint length $L = 60$ mm and blast hole distance $D = 50$ mm maintained constant, change the inclination angle of Joint A α as 0°, 30°, 45°, 60°, and 90°;

(3) Fix the joint length L as 80 mm and inclination angle α as 90°, take blast hole distance D in 25 mm, 50 mm, 70 mm, 90 mm, and 100 mm.

3.3 Results of numerical experiment

3.3.1 Fracture patterns and stress distribution

For the case of $L = 80$ mm, $\alpha = 90°$, and $D = 50$ mm, the evolution of crack growth paths, maximum shear stress, and maximum principal stress fields during blasting is presented in Fig. 5. The blasting fracture process is characterized by four stages, namely the compressive, crushing, propagating, and failure stages. As shown in Fig. 5a, the shock wave generated by the explosion initially causes extensive plastic deformation in the radial direction due to the high strength of the rock, resulting in compressive failure. This deformation leads to the formation of a compressive crushed zone near the blast hole in stage I ($t = 15.998$ µs). As the blasting loads increase ($t = 15.998$–23.796 µs), the stress wave propagates to Joint B, leading to a reflected tensile wave. The low tensile strength of the rock induces plastic tensile deformation, forming a tensile failure zone between the blast hole and Joint B. Stress waves that are not affected by the joints propagate along the specimen, forming the main crack, which propagates radially. When the stress wave reaches the tip of Joint B, a difference in deformation on both sides leads to a deformation gradient at the joint ends, causing a tensile shear crack. Three radial and two wing cracks propagate along the axial direction in stage III ($t = 67.996$ µs) as the stress wave attenuates. Finally, the stress waves and damaged cracks reach the surface, and the cracks branch after
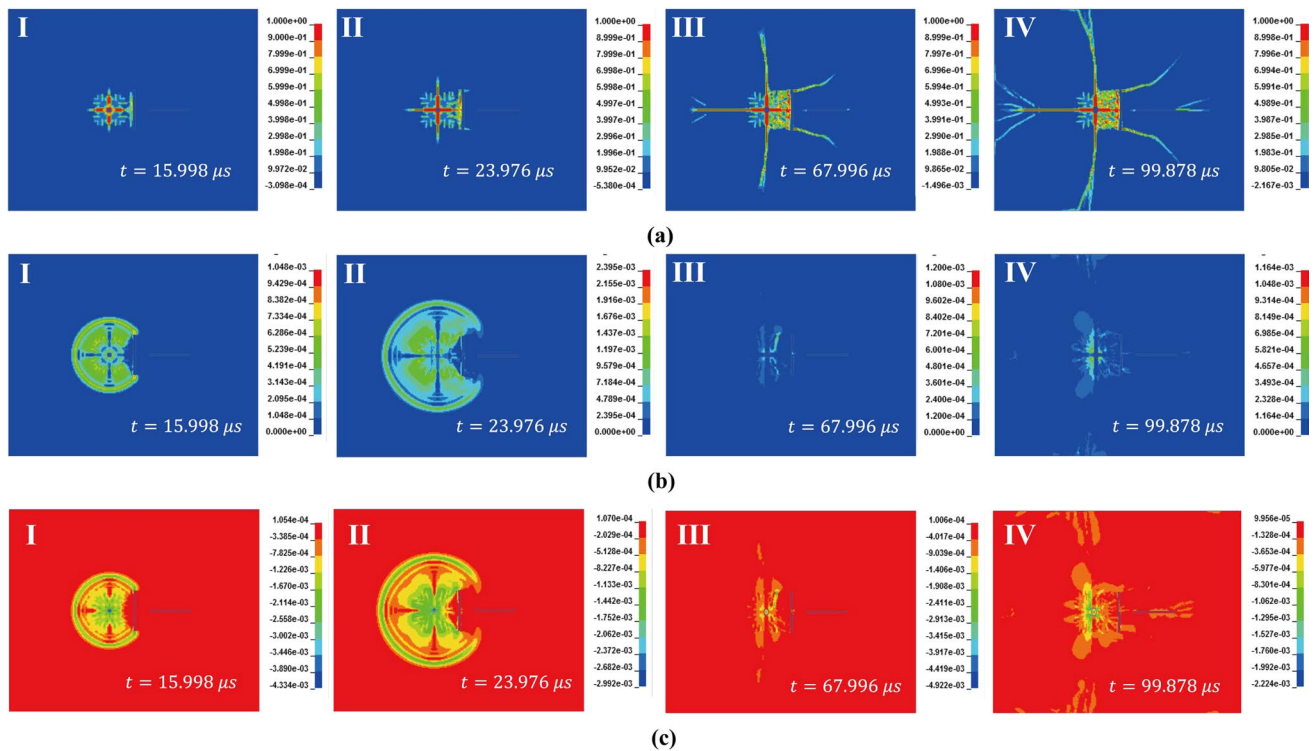
Fig. 5 The spatiotemporal distribution of **a** crack growth paths; **b** maximum shear stress fields (unit: MPa); and **c** maximum principal stress fields (unit: MPa) at different stages
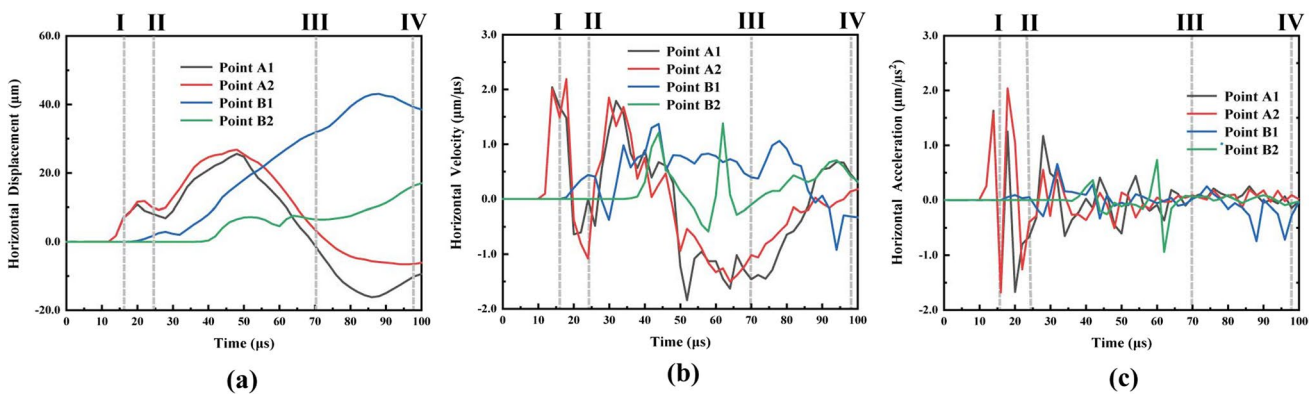

Fig. 6 Evolution of **a** horizontal displacement, **b** horizontal velocity, and **c** horizontal acceleration at the monitoring points in numerical simulations

propagating a certain distance due to the coalescence of the stress waves, as shown in Fig. 5. The transmitted wave leads to the production of two bifurcated cracks at the right end of Joint B.

The data from the monitoring points in the granite specimen during the failure process are shown in Fig. 6. Four representative stages of the failure process are plotted in the history curves. The results show that points A1 and A2 have similar trends due to their symmetry. When the stress wave reaches Joint A, the monitoring points A1 and A2 both

produce rightward horizontal displacements and reach peak values at 25.6 μs. As the stress wave propagates, the horizontal displacement at these points changes from positive to negative, indicating the formation of a reflected tensile wave. However, the displacements of points B1 and B2 show a monotonically increasing trend. Figure 6b shows the horizontal velocity of the monitoring points. The velocity of points A1 and A2 reaches a peak value of 2.04 (μm/μs) at 13.9 μs and then drops to state II due to the rebound effect. The stress wave then converges again, and the velocity of
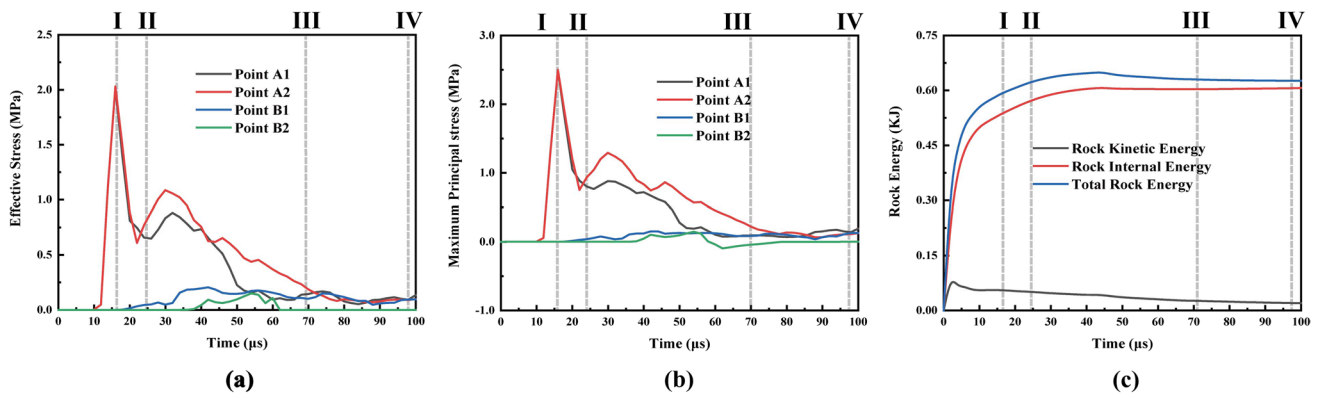
Fig. 7 The evolution process of **a** effective stress, **b** maximum principal stress, and **c** rock energy in granite under the blasting conditions

the two measuring points increases significantly, reaching the peak value again. The same trend can also be observed for monitoring points B1 and B2, but with a time hysteresis.

The effective stress and maximum principal stress at the monitoring points recorded in the simulation are plotted in Fig. 7a, b, respectively. The stress attenuation is clearly visible, and the history curves of the two stresses have the same characteristic. The stress peaks at about 2.0 MPa at point A, while at point G, the peak stress drops to below 0.2 MPa. This indicates the shielding effect of joints on the propagation of stress waves. The recorded strain energy and kinetic energy history are shown in Fig. 7c. The elastic strain energy rises rapidly at the initial load due to the high pressure of the blasting load. With further loading, the kinetic energy

decreases gradually, while the strain energy tends to a constant value of 0.6 kJ.

The peak stress response at various locations under different front joints is as follows: at the A1 end, it occurs within the range of 5–10 μs; at the A2 end, it manifests at approximately 7–8 μs; at the B1 end, it peaks between 19 and 24 μs; and at the B2 end, it reaches its maximum around 38–39 μs. Similarly, for different front joint angles, the peak stress at the A1 end is observed within 4–6 μs, while at the A2 end it ranges from 18 to 20 μs. At the B1 end, it occurs between 20 and 24 μs, and at the B2 end, it is observed at approximately 37–40 μs. In terms of blasting hole spacing, the peak stress at the A1 end of the joint spans from 6 to 23 μs, at the A2 end it ranges from 7 to 24 μs, at the B1 end it falls between
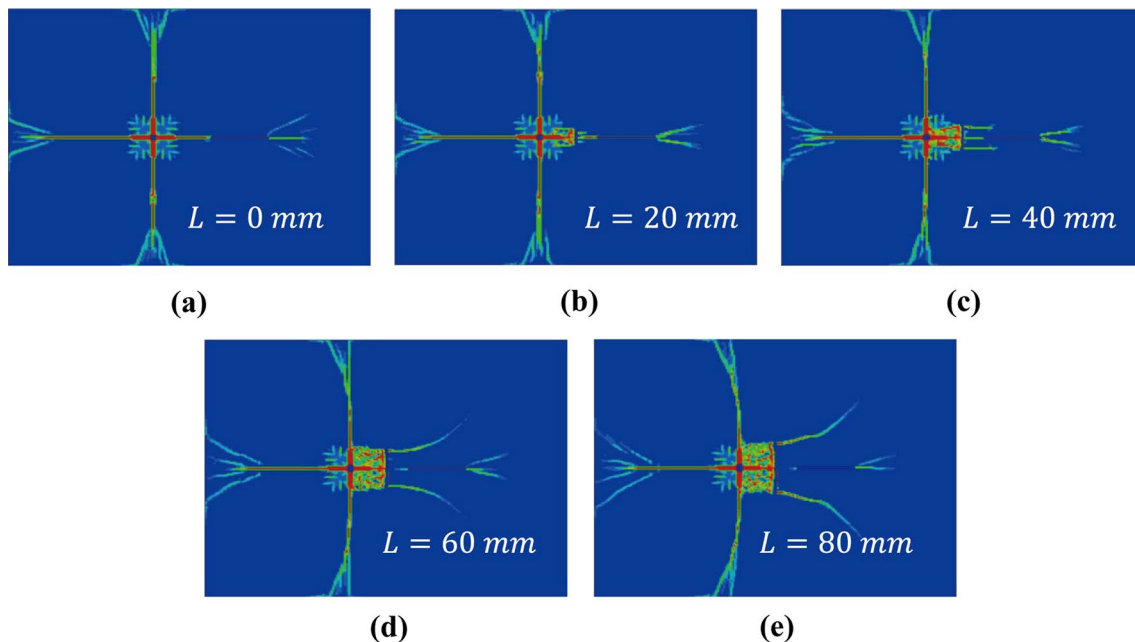
Fig. 8 Ultimate failure patterns after blasting of rock specimens with different joint length L: **a** $L = 0$ mm, **b** $L = 20$ mm, **c** $L = 40$ mm, **d** $L = 60$ mm, and **e** $L = 80$ mm

45 and 50 μs, and at the B2 end it is recorded within the range of 57–60 μs.

### 3.3.2 Blasting with different joint length

To study the influence of the length L of Joint A on mechanical and failure characteristics, we compared the numerical results of five jointed granite specimens with the same configuration except for L, as shown in Fig. 8. It can be observed from Fig. 8 that four main cracks in the shape of a cross are initiated and grow. When the main crack propagates in the opposite direction of Joint A, the crack is hardly affected by the joint, and a branching phenomenon is inclined to occur at the adjacent boundary. A similar phenomenon can be observed for those main cracks that propagate perpendicular to the joint direction, except that the crack propagation direction is deflected as the length of Joint A increases. Crack initiation is observed at different time intervals within the system: the crack in the crushed zone occurs at 3.89 μs, followed by cracks at 6 μs, the joint zone at 12 μs, and finally at 18 μs.

A significant difference was found when the main crack impinges on the prefabricated joints. When the length of Joint A is set to 0 mm (i.e., no front joint exists), the main crack propagates directly along Joint B and bifurcates at the end of Joint B. When the length of the joint is 20 mm, the stress wave generates a reflected tensile wave and a transmitted wave when it reaches Joint A. The reflected tensile wave induces many microcracks and forms a triangular ring crack zone (Friedrich and Schlarb 2011) on the joint surface, while the transmitted wave allows the main crack to further propagate to Joint B in the original direction. As the joint length increases to 40 mm, this phenomenon becomes more pronounced: the ring crack zone becomes larger and connects with the blast hole. Furthermore, as shown in Fig. 8c, two horizontal cracks propagate from the end of Joint A. When the joint length is increased to 60 or 80 mm, the transmission of the main crack becomes less evident, although the bifurcation of the crack can still be observed at the end of Joint B. The triangular ring crack zone formed by the microcracks gradually increases into a rectangle during this stage. Furthermore, the inclination of the wing cracks becomes larger with increasing joint length due to the deflection of the stress wave propagation direction.

3.3.3 Blasting with different joint inclination

Crack propagation and joint interaction are simulated for five different inclination angles (0°, 30°, 45°, 60°, and 90°) of Joint A, as shown in Fig. 9. When Joint A and Joint B are in contact ($\alpha = 0°$), the main crack propagates along the joints and bifurcates at the end, similar to the result in the case of $L = 0$ mm. For an inclination angle of 30°, more radial cracks are formed due to the uniform energy distribution, as shown in Fig. 9. The upper wing end of Joint A is located in the crushed zone, and no evident crack propagation is observed. However, the main crack is shifted towards Joint A under the influence of this joint end, while the stress wave releases from the lower wing end, creating a more extended wing crack. The main crack generated through the
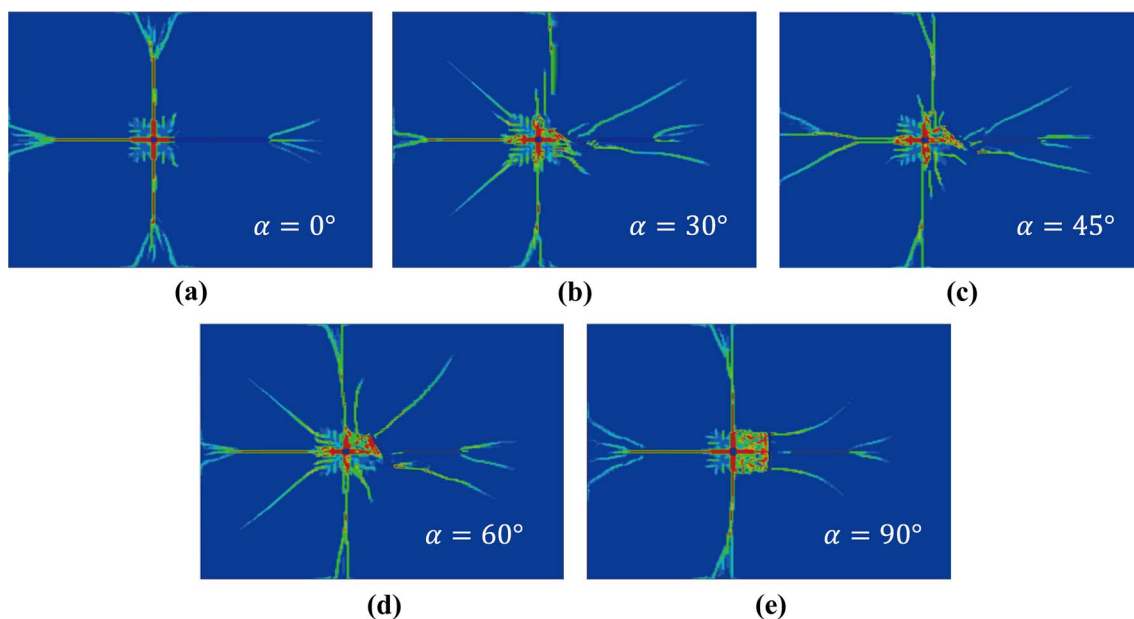
Fig. 9 Ultimate failure patterns after blasting of rock specimens with different inclination angle α of Joint A: **a** $\alpha = 0°$, **b** $\alpha = 30°$, **c** $\alpha = 45°$, **d** $\alpha = 60°$, and **e** $\alpha = 90°$
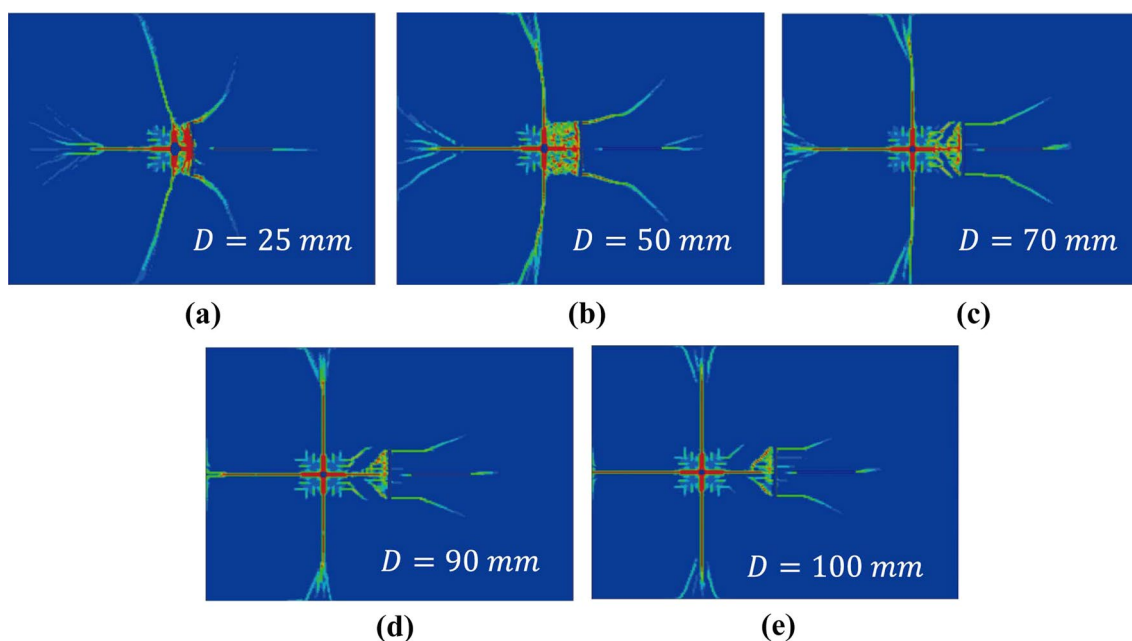
Fig. 10 Ultimate failure patterns after blasting of rock specimens with different blast hole distance D: **a** $D = 25$ mm, **b** $D = 50$ mm, **c** $D = 70$ mm, **d** $D = 90$ mm, and **e** $D = 100$ mm

transmitted wave is deflected in the joint's vertical direction due to the effect of Joint A, but a small crack is still observed from Joint A to Joint B. Increasing the inclination angle α leads to a transition of the main crack from deflection to penetration, as observed from Fig. 9. Results from the case with an inclination of 30° are almost identical to those observed from the case of $\alpha = 60°$ due to rotational symmetry. However, no additional main cracks were found in the case of $\alpha = 45°$. As the number of main cracks increases with the loading rate, it can be inferred that when the inclination angle is at a certain angle, the stress wave reflected by Joint A will enhance the intensity of shock waves around the blast hole.

3.3.4 Blasting with different distance from joint

Figure 10 illustrates the ultimate failure patterns resulting from blasting at five different blast hole distances D from Joint A, specifically 25 mm, 50 mm, 70 mm, 90 mm, and 100 mm. As shown in Fig. 10, the propagation direction of the vertical main crack is deflected by the reflected tensile wave generated by Joint A. This effect gradually diminishes as the blast distance increases. During this process, the inclination angle of the wing crack continuously decreases due to the reduction in blast hole and Joint A tip angle. Furthermore, a significant difference exists in the results of the ring cracks zone between the blasting hole and Joint A at different blast hole distances D. At a distance of 25 mm,

the explosion shock wave interacts with the reflected tensile wave generated by Joint A, resulting in violent microcracks. As this distance increases, the intensity of damage gradually decreases. When the distance reaches 70 mm, the interaction between these two waves begins to decay, demonstrating the spatial independence of the crushed zone and the ring cracks zone. Moreover, when the blasting distance is set to 25 mm, the crushed zone is observed at 12 μs, followed by the appearance of the main crack at 22 μs. As the blasting distance increases, the development time of these two cracks is observed to be delayed. Specifically, at a blasting distance of 100 mm, a crushed zone is observed at 30 μs, with the main crack appearing at 34 μs.

4 Discussion

4.1 Ultimate failure mode

Previous research (Hino 1956; Friedrich and Schlarb 2011) has identified four failure modes near the blast hole that contribute to the rock failure morphology in numerical simulations: the Crushed zone, Ring cracks zone, Main crack (Long radial crack), and short Radial crack. The present study investigated the effects of joints on the blast-induced failure patterns of jointed granite specimens, and three typical ultimate failure patterns were identified, as shown in Fig. 11.
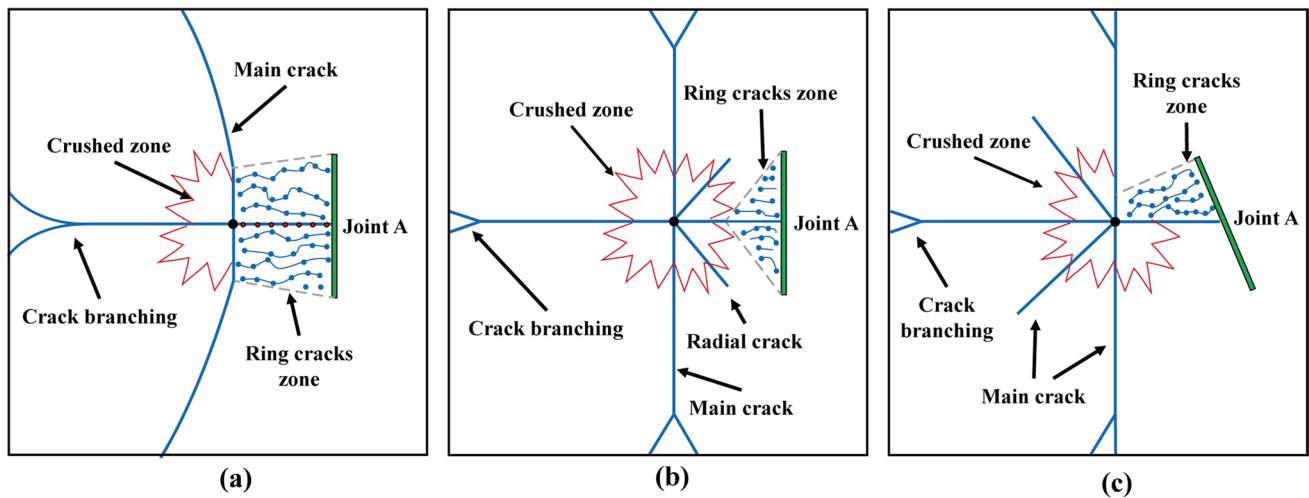
Fig. 11 Three different ultimate failure patterns near the blast hole under the influence of **a** adjacent joint, **b** distant joint, and **c** inclined joint
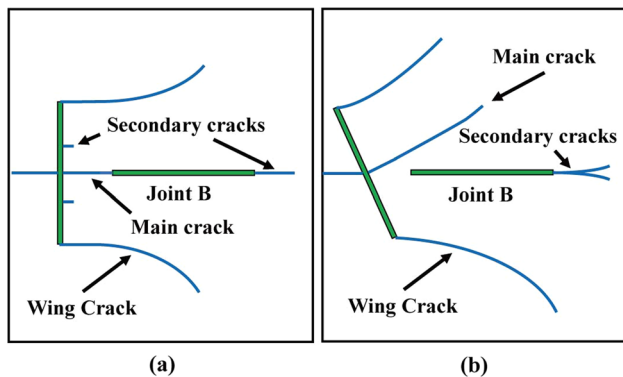

Fig. 12 Failure modes and responses of prefabricated joints to main crack impact with **a** vertical joint and **b** inclined joint

When a joint is located adjacent to the blast hole, the reflected tensile waves generated by the joint can significantly increase the degree of fragmentation near the blast. This effect is manifested by the deflection of the main crack towards the direction of the reflected wave, and the formation of a complete ring cracks zone between the crushed zone and the joint, as shown in Fig. 11a. It is worth noting that the dynamic disturbance of the stress wave at the main crack tip during the propagation process usually bifurcates the main crack, but this effect is suppressed by the reflected tensile wave. When the joint is far from the blast hole, the main crack will no longer deflect since the reflected wave is dissipated in a long propagation path. In this case, the ring cracks zone is formed only on the joint surface. However, there is still a weakened reflected wave that interacts with the crushed zone and forms a short radial crack, as shown in Fig. 11b. When the joint is arranged at a specific angle, additional main cracks can be observed under the disturbance of the stress wave reflected from the joint. Furthermore, due to the effective blast hole distance gradually increasing, the joint only forms a ring cracks zone on the side close to the blast hole.

On the other hand, the failure modes of the main crack impinging and the response of the rear joint are summarized in Fig. 12. It can be observed that when the main crack impinges on the joint surface, a portion of the stress wave can transmit through the surface, resulting in the penetration of the main crack. As the inclination of the joint increases, the main crack will deflect according to the wave interface refraction. However, the propagation of the main crack behind the joint is weaker than in other directions, whether in deflection or penetration. The existence of joints blocks a part of the blasting energy in the form of reflected waves, thus creating a shield effect (Hao et al. 2001; Hutchinson 1987). In addition, some slight secondary cracks initiated from the joints instead of the main crack. Furthermore, the original shear force caused by the difference in stress wave paths on both sides of the joint end will produce a wing crack at the joint ends. According to the experimental results, it was found that the propagation direction of the wing crack is consistent with the direction of the joint end and the blast hole.

4.2 Effect of joint arrangements

Figure 13 displays the peak displacement, velocity, and acceleration of the monitoring points for granite specimens with varying joint lengths L. The peak displacement of both joint ends decreases as joint length increases, but this effect is limited as most of the displacement is caused by global separation of the specimen after main crack propagation rather than local deformation under shock waves. In contrast,
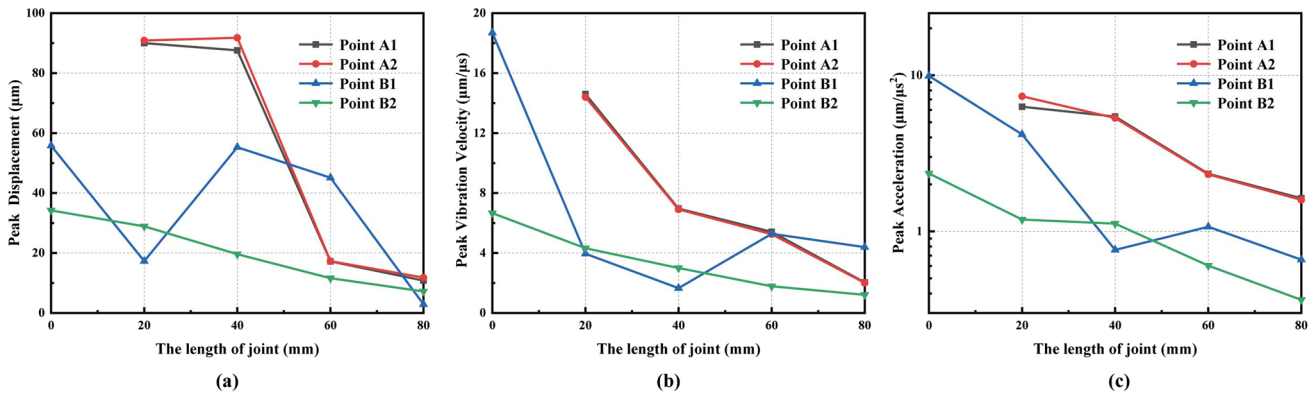
Fig. 13 Effect of the joint length L on **a** peak displacement, **b** peak vibration velocity, and **c** peak acceleration of the monitoring points under the blasting conditions
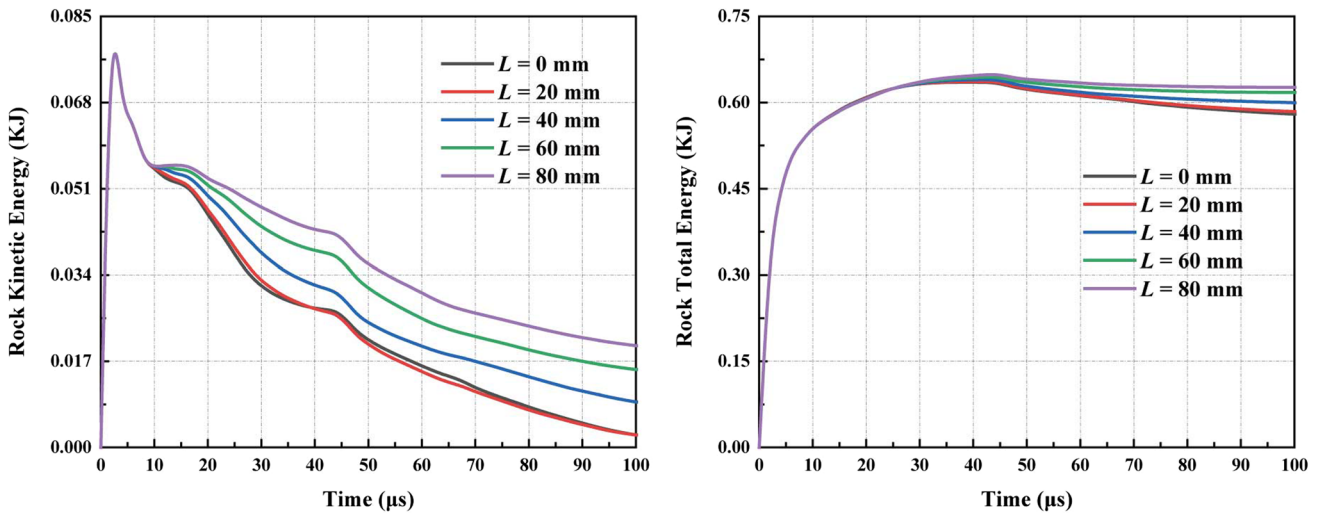

Fig. 14 The evolution process of **a** the rock kinetic energy and **b** rock total potential energy in granite specimens under blasting conditions with different joint length L
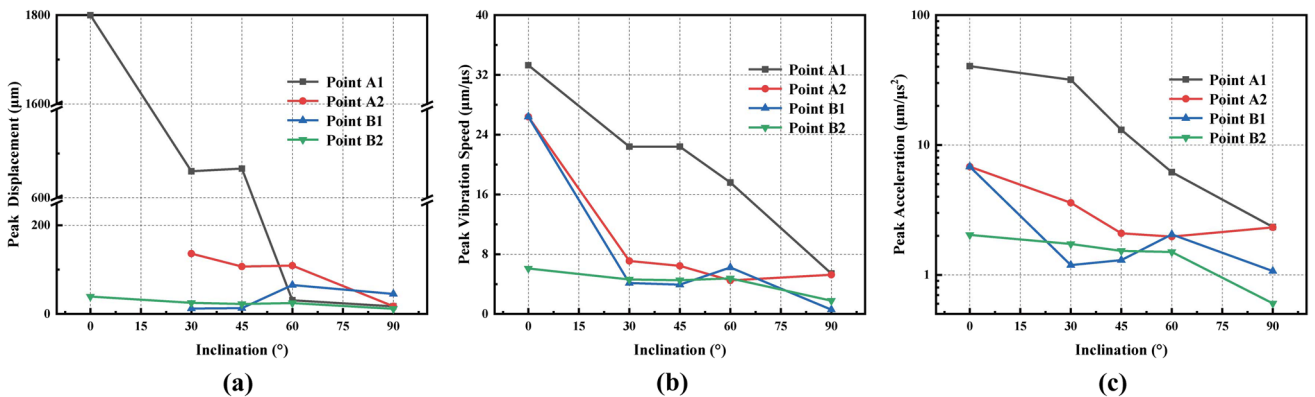

Fig. 15 Effect of the joint inclination α on **a** peak displacement, **b** peak vibration velocity, and **c** peak acceleration of the monitoring points under the blasting conditions

the velocity and acceleration show more significant changes. Comparing point B for cases with $L = 0$ and $L = 20$, a shield effect can be observed, where the peak acceleration at the joint end can be reduced from 9.8 to 7.5 μm/μs² by adding a vertical joint. This suggests that vertical joints can effectively reduce the impact of shock waves at joint ends compared to horizontal joints. When joint length increases to 40 mm, the impact disturbance of Joint B can be reduced to one-tenth of the direct impact case.

Figure 14 shows the recorded kinetic energy and total potential energy history of five granite specimens for joint length study. The energy history curves in each model are consistent in the stage before the stress wave is propagated to the joints (0–10 μs). The kinetic energy decreases after reaching a peak value of 0.914 kJ, a process involving dissipation for crack formation and absorption by the boundary.
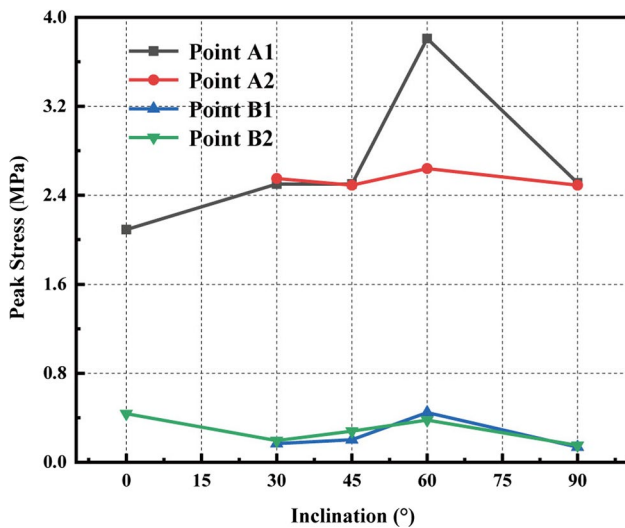
As shown in Fig. 14a, the larger the L value, the smaller the decrease in the kinetic energy of the rock. The total energy of the rock reaches saturation after a certain period of accumulation and tends to be stable, as seen in Fig. 14b. The rock's total energy does not change much for different joint lengths.

Figure 15 presents the effects of joint inclination α on the peak displacement, vibration velocity, and acceleration of monitoring points for granite under blasting conditions. It can be observed in Fig. 15a that point A1 shows singular displacement because it is located in the crushed zone. As the joint inclination α increases, the peak displacement of the wing end of Joint A decreases steeply, while the peak displacement of the end of Joint B remains relatively stable. When α is set to 0°, the velocity and acceleration of each point are the largest, indicating that a joint along the direction of stress wave propagation is disadvantageous. As the angle of Joint A increases, the peak velocity and acceleration both gradually decrease. Moreover, an increase in the inclination angle causes point A1 to gradually move away from the blast hole, while the opposite occurs for point A2. Therefore, the attenuation of point A1 is more significant than that of point A2 during angle changes, as shown in Fig. 15c. It can be concluded that a joint perpendicular to the propagation direction of the stress wave can provide the best shield effect for the rear joint.

To further demonstrate the shield effect of joints, Fig. 16 plots the peak stress of four monitoring points with different joint inclination α. It can be seen that the peak stress at the measuring point of Joint A end ranges from 2.08 to 3.81 MPa. In contrast, the peak stress observed on Joint B is only 0.48 MPa, approximately one-fifth of that on Joint A. In addition, unlike the findings in Fig. 15, the peak stress of different monitoring points is not affected by joint inclination α.
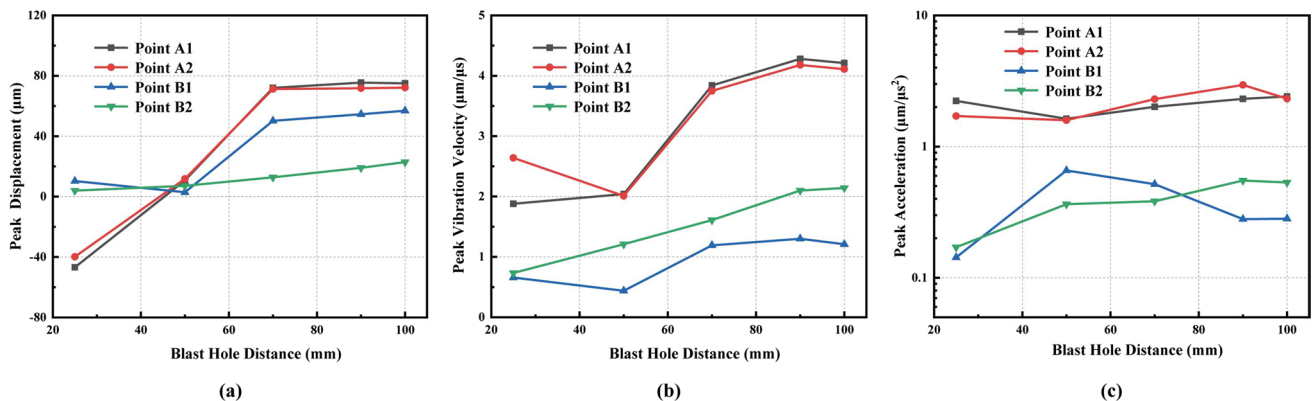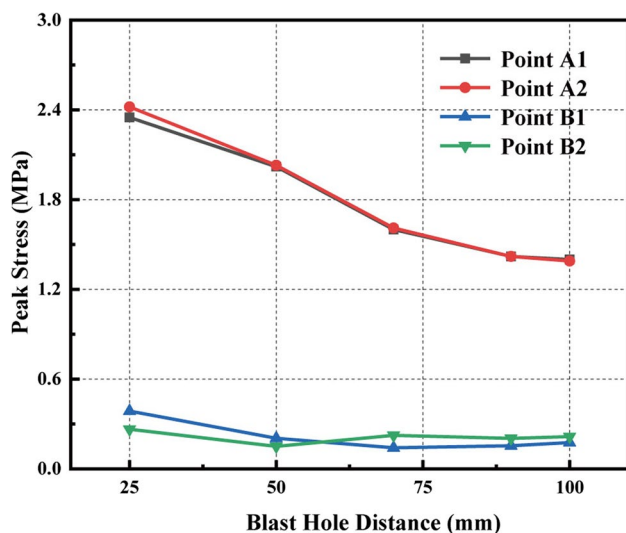

Fig. 16 The peak stress of monitoring points with respect to joint inclination α

Fig. 17 Effect of the blast hole distance D on **a** peak displacement, **b** peak vibration velocity, and **c** peak acceleration of the monitoring points under the blasting conditions

Fig. 18 Effect of the blast hole distance *D* on the peak stress of granite specimens

4.3 Effect of distance from joint

To gain a better understanding of the effects of blast hole distance *D* on the mechanical behavior of jointed granite specimens under blasting conditions, Fig. 17 shows the peak displacement, vibration velocity, and acceleration of the monitoring points. It can be observed that the displacement of the jointed end increases with increasing blast hole distance. A snap-back caused by the reflected tensile wave can be observed at the end of joint A when the blast hole distance is set to 25 mm, resulting in a reverse displacement of 40 μm. For the case where *D* is set as 50 mm, the displacements of four points are similar, indicating that the two joints and the nearby rock mass are displaced as one fragment.

The monitoring results of peak stress in the cases with different blast hole distances are depicted in Fig. 18. It can be observed that as the blast hole distance *D* increases from 25 mm, the peak stress of points A1 and A2 decreases, while the values of points B1 and B2 remain stable. The results obtained in the study indicate that the effect of blasting load on Joint A decreases with increasing blasting distance, while Joint B is not affected by this process in any significant way.

5 Conclusions

In this study, the mechanical behavior of crack propagation and distribution of the stress wave in jointed rock mass under blasting load were numerically explored with the RHT model. The RHT model parameters were calibrated by comparing the result with a single-hole blasting test,

based on previous experiments on granite. Subsequently, we performed simulations on three groups of double-jointed numerical specimens with varying joint arrangements, including joint length (*L*), joint inclination angle (*α*), and blast hole distance (*D*), while subjecting them to blasting loads. By analyzing the numerical calculation results, the following conclusions can be drawn:

(1) The numerical calculations provide valuable insights into the various ultimate failure patterns observed in granite models subjected to blast loading. In addition to the main crack and crushed zone observed in single-hole blasting tests, the numerical simulations reveal the formation of ring crack zones and short radial cracks between the crushed zone and the joint. These formations occur due to the influence of the reflected tensile wave generated by the joint, which disrupts the propagation direction and number of main cracks. Furthermore, the propagation of the shock wave through the front joint gives rise to wing cracks, main cracks, and secondary cracks behind the joints in the numerical results. Upon encountering the front joint, the main crack deflects and penetrates depending on the joint's inclination. While a significant portion of the energy is absorbed or reflected by the front joint, a fraction of the stress wave still reaches the subsequent joint and induces secondary cracks. Moreover, shear stress at the joint's end initiates wing cracks that propagate along the blast hole and the direction of the joint tip.

(2) The numerical test reveals significant vibration isolation effects of vertical joints on stress waves. The presence of longer joints exhibits a noticeable shield effect on rear joints. The inclination angle of Joint A influences the extent of the failure zone: larger inclination angles result in increased reflection of stress waves, leading to more pronounced reflected tension waves and the promotion of microcracks in the ring cracks zone. Moreover, by adjusting the inclination of Joint A, the number of main cracks can be controlled. Furthermore, the effect of the blasting load on Joint A diminishes as the blasting distance increases, while Joint B remains unaffected during this process. Simultaneously, the ring cracks zone induced by the reflected tensile wave diminishes as the stress wave propagation distance increases.

References

Ainalis D, Kaufmann O, Tshibangu J-P, Verlinden O, Kouroussis G (2017) Modelling the source of blasting for the numerical simulation of blast-induced ground vibrations: a review. Rock Mech Rock Eng 50:171–193

Alia A, Souli M (2006) High explosive simulation using multi-material formulations. Appl Therm Eng 26:1032–1042

Banadaki MD, Mohanty B (2012) Numerical simulation of stress wave induced fractures in rock. Int J Impact Eng 40:16–25

Borrvall T, Riedel W (2011) The RHT concrete model in ls-dyna. In: Proceedings of the 8th European LS-DYNA user conference

Chao Z, Ma G, Wang M (2020) Experimental and numerical modelling of the mechanical behaviour of low-permeability sandstone considering hydromechanics. Mech Mater 148:103454

Chen X, Zhao X, Wang H, Ma L, Wang C (2018) Model tests and application research on propagation laws of blasting stress wave in jointed and filled rock mass. J Saf Sci Technol 14:130–134

Chi LY, Zhang Z-X, Aalberg A, Yang J, Li CC (2019) Measurement of shock pressure and shock-wave attenuation near a blast hole in rock. Int J Impact Eng 125:27–38

Daehnke A, Rossmanith H, Napier J (1997) Gas pressurisation of blast-induced conical cracks. Int J Rock Mech Min Sci 34:263-e1

Dai F, Chen R, Iqbal M, Xia K (2010) Dynamic cracked chevron notched Brazilian disc method for measuring rock fracture parameters. Int J Rock Mech Min Sci 47:606–613

Dai J, Yang J, Yao C, Hu Y, Zhang X, Jiang Q, Zhou C (2022) Study on the mechanism of displacement mutation for jointed rock slopes during blasting excavation. Int J Rock Mech Min Sci 150:105032

Friedrich K, Schlarb AK (2011) Tribology of polymeric nanocomposites: friction and wear of bulk materials and coatings. Elsevier

Gharehdash S, Barzegar M, Palymskiy IB, Fomin PA (2020) Blast induced fracture modelling using smoothed particle hydrodynamics. Int J Impact Eng 135:103235

Hajibagherpour A, Mansouri H, Bahaaddini M (2020) Numerical modeling of the fractured zones around a blasthole. Comput Geotech 123:103535

Hallquist JO et al (2006) Ls-dyna theory manual. Livermore Softw Technol Corp 3:25–31

Hao H, Wu Y, Ma G, Zhou Y (2001) Characteristics of surface ground motions induced by blasts in jointed rock mass. Soil Dyn Earthq Eng 21:85–98

He C, Chen D, Xiao J, Lu L, Guo Z (2021) Experimental study of crack propagation and failure around a horseshoe tunnel during nearby blasting. Int J Rock Mech Min Sci 139:104628

Hino K (1956) Fragmentation of rock through blasting and shock wave theory of blasting. In: The 1st US symposium on rock mechanics (USRMS). OnePetro

Hongtao L, Zhiqiang W, Qiang Y et al (2015) Study of dynamic characteristics and blasting crack propagation of quartz mica schist. Chin J Rock Mech Eng 34:2125–2141

Huang X, Qi S, Williams A, Zou Y, Zheng B (2015) Numerical simulation of stress wave propagating through filled joints by particle model. Int J Solids Struct 69:23–33

Hutchinson JW (1987) Crack tip shielding by micro-cracking in brittle solids. Acta Metall 35:1605–1619

Jayasinghe LB, Shang J, Zhao Z, Goh A (2019) Numerical investigation into the blasting-induced damage characteristics of rocks considering the role of in-situ stresses and discontinuity persistence. Comput Geotech 116:103207

John R, Antoun T, Rajendran A (1992) Effect of strain rate and size on tensile strength of concrete. In: Shock compression of condensed matter 1991. Elsevier, pp 501–504

Johnson GR, Holmquist TJ (1994) An improved computational constitutive model for brittle materials. In: AIP conference proceedings, vol 309. American Institute of Physics, pp 981–984

Li H (2016) The study of the rock RHT model and to determine the values of main parameters. China University of Mining & Technology-Beijing, Beijing

Li J, Ma G (2010) Analysis of blast wave interaction with a rock joint. Rock Mech Rock Eng 43:777–787

Li P, Zhou J, Li Z (2018) Blasting stress wave in layered jointed rock mass: propagation law and numerical simulation. J Yangtze River Sci Res Inst 35:97

Li X, Zhu Z, Wang M, Xiao D, Shu Y, Deng S (2021) Fracture mechanism of rock around a tunnel-shaped cavity with interconnected cracks under blasting stress waves. Int J Impact Eng 157:103999

Liu J, Qu S (2014) Experimental study of influence of joint angle of strike on explosive stress wave propagation. Blasting 31:57–61

Liu K, Li X, Hao H, Li X, Sha Y, Wang W, Liu X (2019) Study on the raising technique using one blast based on the combination of long-hole presplitting and vertical crater retreat multiple-deck shots. Int J Rock Mech Min Sci 113:41–58

Liu X, Song S, Tan Y, Fan D, Ning J, Li X, Yin Y (2021) Similar simulation study on the deformation and failure of surrounding rock of a large section chamber group under dynamic loading. Int J Min Sci Technol 31:495–505

Liu S, Wang Z, Zhang Y, Kou M, Bi J (2022) The phase-field simulations of blasting failure in granites. Int J Impact Eng 167:104274

McHugh S (1983) Crack extension caused by internal gas pressure compared with extension caused by tensile stress. Int J Fract 21:163–176

Ming C, Wen-bo L, Chuang-bing Z, Yi L (2009) Influence of initial in-situ stress on blasting-induced cracking zone in tunnel excavation. Rock Soil Mech 30:2254–2258

Miranda L, Cantini L, Guedes J, Binda L, Costa A (2013) Applications of sonic tests to masonry elements: influence of joints on the propagation velocity of elastic waves. J Mater Civ Eng 25:667–682

Raina A (2019) Influence of joint conditions and blast design on pre-split blasting using response surface analysis. Rock Mech Rock Eng 52:4057–4070

Renshu Y, Yanbing W, Dongming G, Huajun X (2016) Experimental research of crack propagation in polymethyl methacrylate material containing flaws under explosive stress waves. J Test Eval 44:248–257

Riedel W, Thoma K, Hiermaier S, Schmolinske E (1999) Penetration of reinforced concrete by beta-b-500 numerical analysis using a new macroscopic concrete model for hydrocodes. In: Proceedings of the 9th international symposium on the effects of munitions with structures, Berlin, vol 315

Rostasy F, Scheuermann J, Sprenger K (1984) Mechanical behaviour of some construction materials subjected to rapid loading and low temperature. Betonwerk Fertigteil Technik 50:393–401

Shu Y, Zhu Z, Wang M, Ying P, Wang F, Wan D, Li X, Gao W (2022) A plastic damage constitutive model for rock-like material focusing on the hydrostatic pressure induced damage and the interaction of tensile and shear damages under impact and blast loads. Comput Geotech 150:104921

Siamaki A, Esmaieli K, Mohanty B (2018) Degradation of a discrete infilled joint shear strength subjected to repeated blast-induced vibrations. Int J Min Sci Technol 28:561–571

Sparks PR, Menzies J (1973) The effect of rate of loading upon the static and fatigue strengths of plain concrete in compression. Mag Concr Res 25:73–80

Torbica S, Lapcevic V (2014) Model for estimating blasted rock fragmentation. Int Multidiscip Sci Geoconf SGEM 3:379

Wang Z, Konietzky H (2009) Modelling of blast-induced fractures in jointed rock masses. Eng Fract Mech 76:1945–1955

Wang Y, Yang R, Ding C, Chen C, Zuo J (2016) Dynamic caustics experiment on crack propagation of defective medium under the effect of explosive stress waves of double holes. J China Coal Soc 41:1755–1761

Wang M, Zhu Z, Dong Y, Zhou L (2017) Study of mixed-mode i/ii fractures using single cleavage semicircle compression specimens under impacting loads. Eng Fract Mech 177:33–44

Wang Z, Huang Y, Xiong F (2019) Three-dimensional numerical analysis of blast-induced damage characteristics of the intact and jointed rock mass. Comput Mater Continua 60:1189–1206

Wang Y, Wen Z, Liu G, Wang J, Bao Z, Lu K, Wang D, Wang B (2020) Explosion propagation and characteristics of rock damage in decoupled charge blasting based on computed tomography scanning. Int J Rock Mech Min Sci 136:104540

Wang B, Li H, Shao Z, Chen S, Li X (2021) Investigating the mechanism of rock fracturing induced by high-pressure gas blasting with a hybrid continuum–discontinuum method. Comput Geotech 140:104445

Wang S, Li J, Li X, He L (2022) Dynamic photoelastic experimental study on the influence of joint surface geometrical property on wave propagation and stress disturbance. Int J Rock Mech Min Sci 149:104985

Wang S, Wang L, Wang Y (2023) Influence of material heterogeneity on the blast-induced crack initiation and propagation in brittle rock. Comput Geotech 155:105203

Xie L, Lu W, Zhang Q, Jiang Q, Chen M, Zhao J (2017) Analysis of damage mechanisms and optimization of cut blasting design under high in-situ stresses. Tunn Undergr Space Technol 66:19–33

Xu P, Yang R-S, Guo Y, Chen C, Kang Y (2021) Investigation of the effect of the blast waves on the opposite propagating crack. Int J Rock Mech Min Sci 144:104818

Yang R-S, Yue Z-W, Dong J-C, Gui L, Xiao T (2008) Dynamic caustics experiment of blasting crack propagation in discontinuous jointed material. J China Univ Min Technol 37:467–472

Yang R, Ding C, Wang Y, Chen C (2016) Action-effect study of medium under loading of explosion stress wave and explosion gas. Chin J Rock Mech Eng 35:3501–3506

Yang J, Yao C, Jiang Q, Lu W, Jiang S (2017) 2d numerical analysis of rock damage induced by dynamic in-situ stress redistribution and blast loading in underground blasting excavation. Tunn Undergr Space Technol 70:221–232

Yi C, Johansson D, Nyberg U, Beyglou A (2016) Stress wave interaction between two adjacent blast holes. Rock Mech Rock Eng 49:1803–1812

Yi C, Johansson D, Greberg J (2018) Effects of in-situ stresses on the fracturing of rock by blasting. Comput Geotech 104:321–330

Yi C, Nordlund E, Zhang P, Warema S, Shirzadegan S (2021) Numerical modeling for a simulated rockburst experiment using ls-dyna. Underground Space 6:153–162

Yuan W, Wang W, Su X, Li J, Li Z, Wen L, Chang J (2018) Numerical study of the impact mechanism of decoupling charge on blasting-enhanced permeability in low-permeability sandstones. Int J Rock Mech Min Sci 106:300–310

Yuan W, Su X, Wang W, Wen L, Chang J (2019) Numerical study of the contributions of shock wave and detonation gas to crack generation in deep rock without free surfaces. J Petrol Sci Eng 177:699–710

Zhang Q, Zhao J (2013) Determination of mechanical properties and full-field strain measurements of rock material under dynamic loads. Int J Rock Mech Min Sci 60:423–439

Zhang F, Peng J, Fan G, Li S, Li Y (2016) Mechanisms of blasting-induced rock fractures under different static stress and joint properties conditions. Rock Soil Mech 37:1839–1846

Zhang Y, Deng H, Deng J, Liu C, Ke B (2019) Peridynamics simulation of crack propagation of ring-shaped specimen like rock under dynamic loading. Int J Rock Mech Min Sci 123:104093

Zhang Z, Gao W, Li K, Li B (2020) Numerical simulation of rock mass blasting using particle flow code and particle expansion loading algorithm. Simul Model Pract Theory 104:102119

Zhang Z-X, Hou D-F, Guo Z, He Z (2020) Laboratory experiment of stemming impact on rock fragmentation by a high explosive. Tunn Undergr Space Technol 97:103257

Zhang Z-X, Qiao Y, Chi LY, Hou D-F (2021) Experimental study of rock fragmentation under different stemming conditions in model blasting. Int J Rock Mech Min Sci 143:104797

Zhu Z, Mohanty B, Xie H (2007) Numerical investigation of blasting-induced crack initiation and propagation in rocks. Int J Rock Mech Min Sci 44:412–424

Zhu Z, Xie H, Mohanty B (2008) Numerical investigation of blasting-induced damage in cylindrical rocks. Int J Rock Mech Min Sci 45:111–121